electronics

MDPI

Article

Data Mining in the Vibration Signal of the Trip Mechanism in Circuit Breakers Based on VMD-PSR

Xuezong Wang [1], Jiangjun Ruan [1,*], Taotao Zhou [2], Xuelin Peng [2], Yongqing Deng [1] and Qiuyu Yang [3]

[1] School of Electrical Engineering and Automation, Wuhan University, Wuhan 430072, China
[2] Wuhan Power Supply Company, State Grid Hubei Electric Power Company, Wuhan 430013, China
[3] School of Electronic, Electrical Engineering and Physics, Fujian University of Technology, Fuzhou 350118, China
* Correspondence: ruan308@126.com

Abstract: To address the difficulty in characterizing early mechanical faults in the trip mechanism of circuit breakers, a data mining method based on variational mode decomposition (VMD) and phase space reconstruction (PSR) method was proposed. First, the vibration signal in the trip stage was separated from the whole according to the current features. Then, it was decomposed using the VMD algorithm to obtain the intrinsic mode functions (IMFs) and these sub signals were mapped to high-dimensional phase space based on the PSR algorithm. Then, the features of the attractor trail shape and the recurrence plot matrixes were extracted. In order to judge the fault in the trip mechanism, a fault simulation test was carried out and the characteristic under different faults was analyzed. Based on these samples, a fault identification model is established by support vector machine (SVM) and the effectiveness is verified by other test samples. The accuracy of the SVM model is 98%, which is higher than that of the BPNN and KNN clustering models. This research supplements the existing method for condition evaluation of the trip mechanism and can provide a reference for circuit breaker fault diagnosis.

Keywords: circuit breakers; vibration signal; variational mode decomposition; phase space reconstruction; fault identification

Citation: Wang, X.; Ruan, J.; Zhou, T.; Peng, X.; Deng, Y.; Yang, Q. Data Mining in the Vibration Signal of the Trip Mechanism in Circuit Breakers Based on VMD-PSR. *Electronics* **2022**, *11*, 3700. https://doi.org/10.3390/electronics11223700

Academic Editors: Ayman El-Hag, Issouf Fofana, Behzad Kordi, Refat Ghunem and Ali Naderian

Received: 31 October 2022
Accepted: 8 November 2022
Published: 11 November 2022

1. Introduction

As an important switchgear equipment in a power system, the safe and stable operation of circuit breakers (CBs) is very important. The trip mechanism composed of a open/close coil circuit as well as a latch is the weak point among CBs. During 2004–2007, 50% of the major failures of CBs came from the operating mechanism including the open/close coil and the latch. Moreover, 30% of the major failures occurred in electrical control and auxiliary circuits, such as open/close circuits and auxiliary switches [1]. Meanwhile, according to the statistical data of China Southern Power Grid, failures in the trip mechanism are a significant cause of misoperation fault in CBs, contributing to 45% of the major failures [2,3]. Therefore, it is of great significance to detect early faults of the trip mechanism so as to ensure the safe and stable operation of the power system.

When the CB receives the open/close signal, the coil circuit in the trip mechanism is turned on and the plunger in the coil pushes the latch under the electromagnetic force, which provides mechanical signals for the subsequent transmission process. The open/close coil current is one of the direct signals that reflect the state of the trip mechanism and is also the one of the main signals presently used in the fault diagnosis of CBs. Relevant research about the coil current focuses on the simulation of the coil current [4,5] and the features extracted from the current waveform for fault diagnosis [6,7]. However, these studies mainly concentrated on the electrical faults of the coil circuit and the mechanical faults of the jam in the open/close latch. There is little research on the coil-plunger jam fault that may cause the failure of the trip mechanism. As the coil-plunger jam fault occurs

throughout the whole trip process, a slight jam could finally lead to failures, where the coil current has not changed significantly. Thus, it is difficult to identify this mechanical fault using only current features.

Vibration signal is a direct reflection of the mechanical condition of equipment, which is widely used in the assessment of health condition. The vibration signal of a CB mainly comes from the mechanical wave generated by the plunger hitting the latch in the trip process, the movement of various components in the transmission process, and the collision of moving contact. The signal contains rich and important mechanical condition information of the CB, which can be used as the basis for fault diagnosis and maintenance [8,9]. Because the vibration signal of the CB has complex structural characteristics in both the time and frequency domain, it is often necessary to decompose it for simplicity. Common vibration signal decomposition methods include empirical mode decomposition (EMD) [10], wavelet transform (WT) [11], and variational mode decomposition (VMD) [12,13]. Among them, VMD processes the signal by solving the variational problem, avoiding the selection of wavelet bases in WT, and can adaptively decompose the signal into quasi orthogonal intrinsic mode functions (IMFs) with different characteristics [14]. In addition, this method avoids the mode mixing problem in EMD and has better performance in analyzing non-stationary signals [15,16].

The vibration signal could be decomposed into sub signals with different modes according to the VMD method, from which the key features reflecting the condition of the CB can be extracted. Relevant studies use the sample entropy [17], arrangement entropy [18], marginal spectral energy entropy [19], and local singular value [12] to extract features from the mode components in the vibration signal and evaluate the mechanical condition of CBs. However, these studies mainly focus on the fault diagnosis of the overall operating mechanism and there is less independent analysis and research on the trip mechanism. SAs the vibration in the trip process mainly comes from the movement of the plunger and the strike on the latch, the energy it contains is far less than the energy of the transmission parts in the transmission process. Moreover, it is earlier than the time at which the contact starts to move, so the vibration signal at this stage is ignored in most works in the literature. Owing to the short duration of this process and the small amount of data, how to reconstruct the signal and extract more information from it is the difficulty of the research.

Therefore, this paper focuses on the trip mechanism, especially the open/close coil in the operating mechanism. Considering the problem that the coil current (CC) is difficult to characterize with the coil-plunger jam, the vibration signal during the trip process is introduced to evaluate the condition of the trip mechanism. In view of the vibration signal with mode mixing, as well as the short duration and insufficient amount of data in the trip process, a vibration signal feature extraction method based on VMD and phase space reconstruction (PSR) was proposed in this paper. First, VMD was used to decompose the vibration signal to obtain the IMFs in different frequency ranges. Then, each IMF was mapped into the high-dimensional phase space based on the phase space reconstruction method, so that features could be extracted. Based on the Pearson correlation coefficient, the dimension of the feature set is reduced and optimized and, combined with a fault simulation test, a fault identification model is established based on support vector machine (SVM). Compared with the identification accuracy of the back propagation neural network (BPNN) and K-nearest neighbor (KNN) clustering method, the effectiveness of the method was verified. The research results enrich the fault diagnosis method of the trip mechanism and can provide a reference for the evaluation of CBs' condition.

2. Data Mining in Vibration Signal Based on VMD-PSR

2.1. Vibration Signal during Trip Process

Taking the open process of the VS1-12 circuit breaker as an example, the measurement test was carried out and is shown in Figure 1 The CC was measured by the hall current sensor. The vibration signal was measured by the acceleration sensor, which was attached to the shell of the operating mechanism. Both the CC and the vibration signals were synchronously received through the acquisition card. The sample rate was set to 100 kHz.

The vibration signal during the whole operating process was collected and compared with the current signal, which is shown in Figure 2. According to the key points of the current signal, the vibration signal can be mainly divided into these parts:

(1) 0~t_1: The acceleration stage of the plunger. The coil circuit is turned on at 0, and the electromagnetic force is generated to accelerate the plunger in the coil. At t_a, the current reaches the peak. During this stage, the vibration signal mainly comes from the friction between the coil and the plunger, whose amplitude is small.

(2) t_1~t_2: The trip process. At t_1, the coil plunger hits the latch and reaches the maximum displacement at t_2. At this stage, the latch is released and the subsequent transmission parts are triggered. In addition to the continuous movement of the plunger, the vibration signal mainly comes from the impact of the plunger on the open latch.

(3) t_2~t_3: Transmission stage. The operating mechanism is unlocked and the moving contact starts to move under the function of the open spring. The vibration signal mainly comes from the collision and movement of various components in the mechanism.

(4) After t_3: Braking stage. At t_3, the transmission is completed and the auxiliary switch is switched, so that the coil circuit is turned off. Strong mechanical waves are generated by the collision of moving contact in the mechanism.

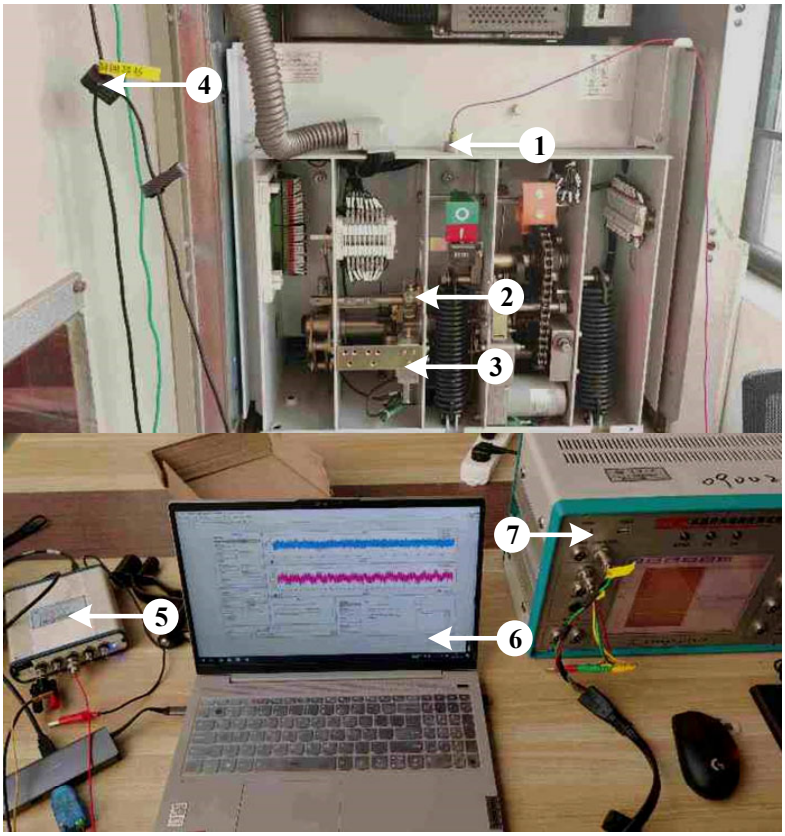

①Acceleration sensor ②Open latch ③Open coil ④Hall current sensor
⑤Acquisition card ⑥Laptop ⑦Power supply

Figure 1. Measurement test of the CC and the vibration signals.

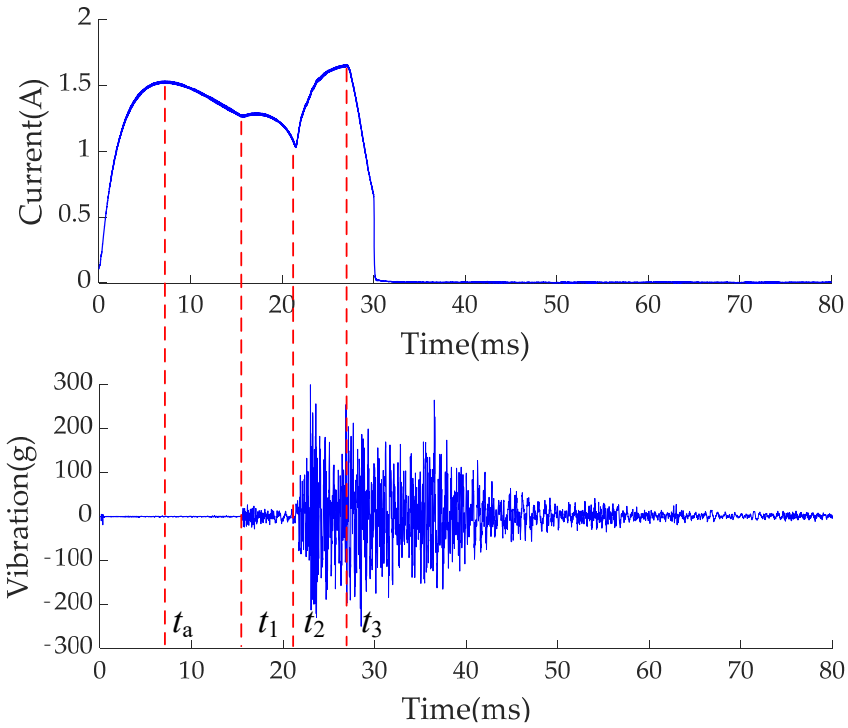

Figure 2. Measurement results of the signals.

In conclusion, it can be seen that the vibration signal during t_1~t_2 is closely related to the condition of the trip mechanism. The signal includes both the components generated by the coil-plunger and the impact on the latch. Relevant signals could be separated from it and features can be extracted to characterize the condition of the circuit as well as the jam between the coil and plunger. Therefore, the vibration signal at this time is taken as the characteristic signal of the trip mechanism.

2.2. VMD Method of the Vibration Signal

The VMD method can decompose a signal $x(t)$ into k discrete modes u_k by iteratively searching the optimal solution in the variational model, and each mode has central frequency ω_k and limited bandwidth. By minimizing the sum of the estimated bandwidth of each mode, the variational problem is constructed to realize the decomposition of the signal. In this paper, the VMD method is used to decompose the vibration signal and the basic principle is expressed as follows [20]:

The original signal $x(t)$ can be decomposed into the following:

$$x(t) = \sum_{k=1}^{K} u_k(t) \tag{1}$$

where K is the decomposition level and $u_k(t)$ is the intrinsic mode function (IMF).

The analytical signal of each mode is calculated by Hilbert transform, so as to obtain the unilateral spectrum of the IMF:

$$[\delta(t) + \frac{j}{\pi t}] * u_k(t) e^{-j\omega_k t} \tag{2}$$

The bandwidth of each IMF signal can be estimated by the two-norm square of the first-order reciprocal of the demodulating signal. Then, the constrained variational model could be built as follows:

$$\min_{\{u_k\},\{\omega_k\}} \left\{ \sum_k \left\| \partial_t [(\delta(t) + \frac{j}{\pi t}) * u_k(t)] e^{-j\omega_k t} \right\|_2^2 \right\} \tag{3}$$

Introducing the Lagrange multiplier $\lambda(t)$ and penalty factors α to solve the variational model,

$$L(\{u_k\},\{\omega_k\},\lambda) = \alpha \sum_{k=1}^{K} \left\| \partial_t [(\delta(t) + \frac{j}{\pi t}) * u_k(t)] e^{-j\omega_k t} \right\|_2^2 + \left\| x(t) - \sum_{k=1}^{K} u_k(t) \right\|_2^2 + \left\langle \lambda(t), x(t) - \sum_{k=1}^{K} u_k(t) \right\rangle \tag{4}$$

u_k, ω_k, and λ are updated by alternating iterations to find the optimal solution of the expression. For the function $u_k(t)$, its iterative calculation formula is as follows:

$$u_k^{n+1} = \underset{u_k}{\operatorname{argmin}} \left\{ \alpha \left\| \partial_t [(\delta(t) + \frac{j}{\pi t}) * u_k(t)] e^{-j\omega_k t} \right\|_2^2 + \left\| x(t) - \sum_{i=1}^{K} u_i(t) + \frac{\lambda(t)}{2} \right\|_2^2 \right\} \tag{5}$$

where u_k^n is the result of the nth iteration of u_k, δ (t) is the Dirac delta function, and * is the convolution operator. By transforming the equation into the frequency domain according to Parseval Fourier isometric transformation and Hermitian symmetric matrix under L2 norm, the iterative calculation formula could be expressed as

$$u_k^{n+1} = \underset{u_k}{\operatorname{argmin}} \left\{ \int_0^{\infty} [4\alpha(\omega - \omega_k)^2 |\hat{u}_k(\omega)|^2 + 2 \left| \hat{x}(\omega) - \sum_{i=1}^{K} \hat{u}_i(\omega) + \frac{\hat{\lambda}(\omega)}{2} \right|^2] \mathrm{d}\omega \right\} \tag{6}$$

The solution of the above quadratic optimization problem can be obtained by seeking the partial derivative, and the iterative formula u_k^{n+1} can be calculated by

$$\hat{u}_k^{n+1} = \frac{\hat{x}(\omega) - \sum\limits_{i \neq k} \hat{u}_i(\omega) + \frac{\hat{\lambda}(\omega)}{2}}{1 + 2\alpha(\omega - \omega_k)^2} \tag{7}$$

Moreover, it can be transformed into the problem of finding the minimum value to obtain ω_k^{n+1}

$$\omega_k^{n+1} = \underset{\omega_k}{\operatorname{argmin}} \left\{ \alpha \left\| \partial_t [(\delta(t) + \frac{j}{\pi t}) * u_k(t)] e^{-j\omega_k t} \right\|_2^2 \right\} \tag{8}$$

Then, by transforming to the frequency domain and seeking the partial derivative, the iterative calculation formula for ω_k^{n+1} is

$$\omega_k^{n+1} = \frac{\int_0^{\infty} \omega |\hat{u}_k(\omega)|^2 \mathrm{d}\omega}{\int_0^{\infty} |\hat{u}_k(\omega)|^2 \mathrm{d}\omega} \tag{9}$$

For λ^{n+1}, its iterative formula could be obtained by the gradient descent method:

$$\hat{\lambda}^{n+1} = \hat{\lambda}^n + \tau_0 [\hat{x}(\omega) - \sum_{i=1}^{K} \hat{u}_i(\omega)] \tag{10}$$

where τ_0 is the Lagrangian multiplier.

As there will be noise included in the measured vibration signal, the Lagrangian multiplier is set to 0. The termination condition of the iterative update is

$$\sum_{k=1}^{K} \left(\left\| \hat{u}_k^{n+1} - \hat{u}_k^n \right\|_2^2 / \| \hat{u}_k^n \|_2^2 \right) < \varepsilon_0 \tag{11}$$

During the process of VMD, the decomposition level K needs to be defined in advance. A small value of K will lead to the failure of mode identification, while a large value of K will lead to mode mixing. In this paper, the optimal parameter of K is determined by the similarity of the central frequency of each IMF. The default value of K is 2. If the central frequencies of adjacent IMFs are not similar, that is, $\omega_k / \omega_{k-1} > 1.2$, then $K = K + 1$. If $\omega_k / \omega_{k-1} < 1.2$, it is judged that there is over decomposition, and the final decomposition level is set to $K - 1$. The VMD process in this paper is shown in Figure 3.

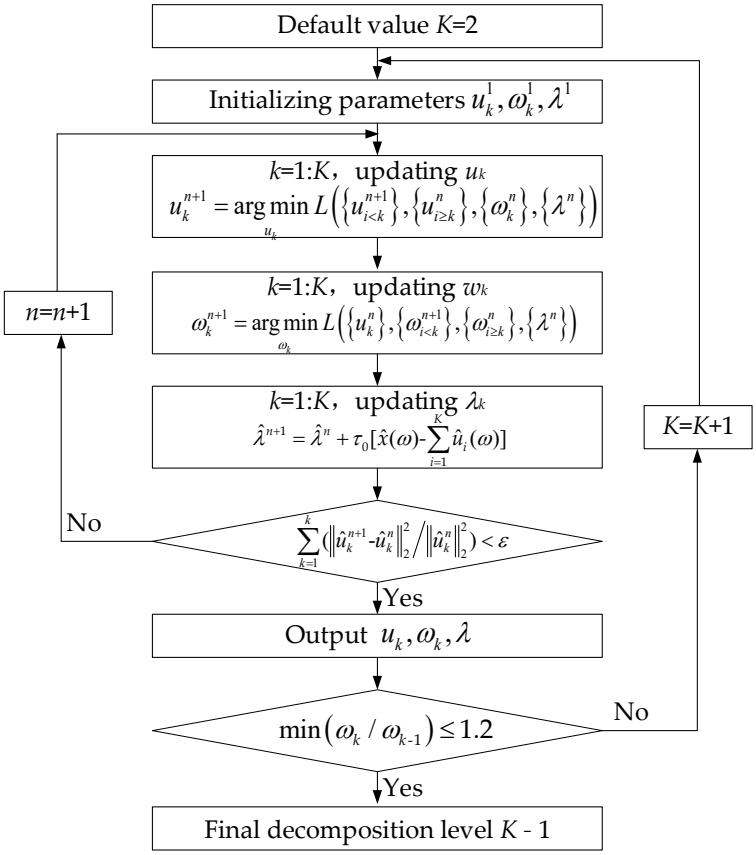

Figure 3. Process of VMD.

Taking the vibration signal at t_1~t_2 in Figure 2 as an example, the optimal decomposition level is 7 and penalty factors α is 1000. The time–frequency domain results of the corresponding IMF1~IMF7 by VMD method are shown in Figure 4. It can be seen that the frequency distribution of IMF1 is within 0~5 kHz, which is a relatively stable and gradually increasing periodic signal in the time domain, corresponding to the vibration of the operating mechanism. The frequency distribution of IMF2~IMF6 is within 5~25 kHz, which are shown as attenuated impact signals in the time domain, corresponding to the vibration of the open latch and related components. Besides, the vibration signal also has a high-frequency component IMF7 with 44 kHz central frequency, which shows a continuous vibration with low amplitude in the time domain, corresponding to the vibration of the open coil.

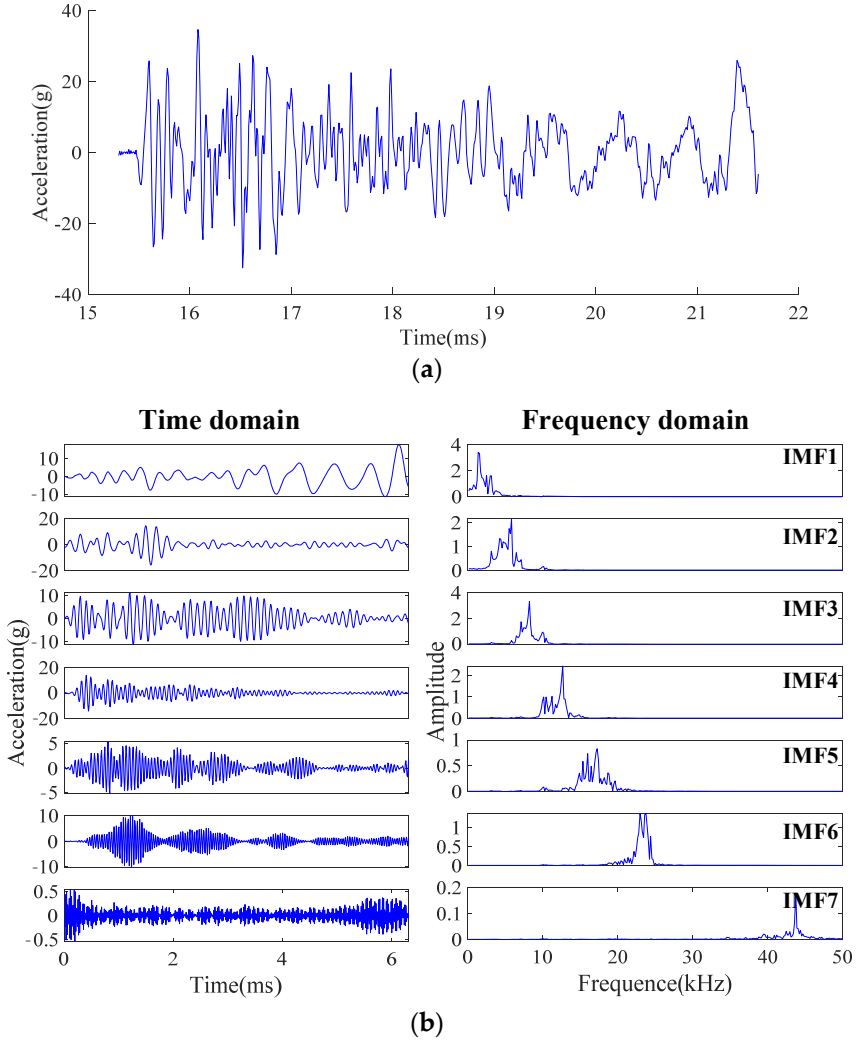

Figure 4. VMD results of the vibration signal. (**a**) Raw signal. (**b**) Time frequency domain results of IMFs.

2.3. PSR Method of the Sub Signals

As the CB is a complex nonlinear system, the vibration signal generated in the trip process contains the evolution information of the CB's dynamic system. Based on the VMD algorithm, the mode components in the trip mechanism can be separated and extracted, but the condition information is still hidden in the IMFs, which needs further mining. PSR has a good effect in dealing with chaotic time series. By extending one-dimensional time series and mapping it to high-dimensional phase space, more information can be extracted from it. In this paper, the PSR method is used for data mining in the IMFs of the vibration signal. For the vibration signal time series $\boldsymbol{x} = \{x(i), i = 1, 2, \ldots, N\}$, by introducing the time interval τ to delay the sequence, an m-dimensional phase space vector can be reconstructed:

$$\begin{aligned} \boldsymbol{X} &= \begin{bmatrix} x(1) & x(2) & \cdots & x[N-(m-1)\tau] \\ x(1+\tau) & x(2+\tau) & \cdots & x[N-(m-2)\tau] \\ \cdots & \cdots & \cdots & \cdots \\ x(1+(m-1)\tau) & x(2+(m-1)\tau) & \cdots & x(N) \end{bmatrix} \\ &= [\boldsymbol{X}(1), \boldsymbol{X}(2), \cdots \boldsymbol{X}(N-(m-1)\tau)] \end{aligned} \tag{12}$$

Each column represents a phase point in the m-dimensional phase space. Thus, the connecting line between $[N-(m-1)\tau]$ phase points constitutes the trail of the system in phase space, which is called the chaotic attractor.

The delay time τ and embedding dimension m determine the effectiveness of the phase space reconstruction. Considering that different IMFs correspond to different central frequencies, the delay time of each IMF in this paper is determined through the center frequency.

$$\tau_k = \frac{1}{6\omega_k} \tag{13}$$

The false nearest neighbour method is used to determine the optimal embedding dimension [21]. When the embedding dimension is low, the phase space is mixed, and some phase points with different labels would be clustered, resulting in the false nearest neighbour points. When the dimension increases, these points will separated gradually. While the embedding dimension is d and $d+1$, the distance between the vector $\boldsymbol{X}(i)$ and its nearest neighbour is

$$\begin{aligned} D_d(i) &= \min\{\|X_d(i) - X_d(j)\|, j \neq i\} \\ D_{d+1}(i) &= \|X_{d+1}(i) - X_{d+1}(j)\| = \sqrt{D_d(i)^2 + \|x(i+d\tau) - x(j+d\tau)\|^2} \end{aligned} \tag{14}$$

If $[D_{d+1}(i) - D_d(i)]/D_d(i) \geq 10$, the corresponding point is the false nearest neighbour point. The minimum embedding dimension m when these points disappear is the optimal value.

According to the above method, the PSR results of the IMFs in Figure 4 are calculated, and the best embedding dimension of these signals is 4. Taking the first two dimensions in the phase space as an example, the results are shown in Figure 5. For IMF1, the attractor trail shrinks to the origin and is irregular. The trails of IMF2~IMF6 are nearly spherical. For periodic vibration signal such as IMF7, it behaves as an alternating motion around the origin in phase space.

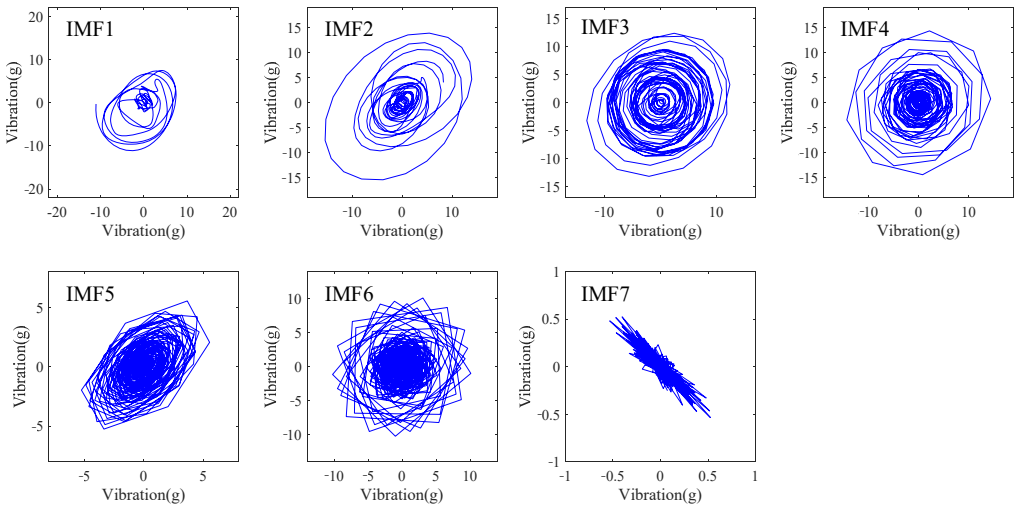

Figure 5. PSR results of the IMFs.

2.4. Feature Extraction from the Vibration Signal

Features about the shape of the attractor trail can be extracted from the phase space [22], which could characterize the vibration signal and is related to the fault condition of the trip mechanism. In this paper, the features such as the trail change speed and the ratio of the major–minor axis are extracted, which are shown in Table 1.

Table 1. Features from the shape of the attractor trail, where m_0 and n_0 are the major and minor axis of the minimum enclosing rectangle of the attractor, respectively, and S is the coverage area.

Feature	Description
$r_{\max}$	Center distance of the attractor, which represents the radius of the minimum circumscribed sphere of the attractor. $r = \max\|X_i\|$
$v_{\max}$	Maximum change speed, which represents the maximum distance between state points in phase space. $v_{\max} = \max\|X_{i+1} - X_i\|$
v_a	Average change speed, which represents the average distance between state points in phase space. $v_a = \sum_{i=1}^{N-(m-1)\tau-1} \|X_{i+1} - X_i\| / [N - (m-1)\tau - 1]$
r_v	Speed ratio, which represents the ratio of the maximum speed to the average speed. $r_v = v_{\max}/v_a$
r_l	Ratio of major–minor axis, which represents the ratio of the major axis to the minor axis of the minimum enclosing rectangle of the attractor. $r_l = m_0/n_0$
r_s	Trail compactness, which represents the ratio of the attractor coverage area to the minimum enclosing rectangle area. $r_s = S/(m_0 n_0)$

In addition, nonlinear time series generated by the dynamic system can be transformed into a two-dimensional plan to describe the internal change law of the dynamic system through the recurrence quantification analysis (RQA) method [23]. For the PSR signal $\boldsymbol{X}$ in Equation (12), the distances between each point in the phase space can be calculated so as to build the recurrence plot (RP) image, and the recurrence matrix is constructed by introducing the threshold:

$$R_{i,j} = \mathrm{sgn}(\varepsilon - \|\boldsymbol{X}(i) - \boldsymbol{X}(j)\|) \tag{15}$$

where sgn is the step function; ε is the threshold, which is equal to 50% of the signal variance in this paper; and $\|\boldsymbol{X}(i) - \boldsymbol{X}(j)\|$ is the Euclidean distance between $\boldsymbol{X}(i)$ and $\boldsymbol{X}(j)$ in phase space.

When $\varepsilon > \|\boldsymbol{X}(i) - \boldsymbol{X}(j)\|$, $R_{i,j} = 1$, and the point in the matrix is the recursive point. Taking the signals in Figure 5 as examples, the RP images of these IMFs are converted into RGB images in Figure 6, and then the recurrence matrix can be calculated from the RP images.

The recurrence plot matrix shows the hidden information in the signal in the form of a two-dimensional image, in which the diagonal structure represents the single frequency periodic motion and the vertical white area reflects the characteristics of the impact components. Quantitative features extracted from the matrix could characterize the vibration signal [24–27]. In this paper, these features are as shown in Table 2, where N_0 is the length of PSR signal, $N_0 = N - (m-1)\tau$. $P(l)$ is the number of diagonals with length l, and $l_{\min} = 2$. $P(v)$ is the number of verticals with length v, and $v_{\min} = 2$. $p(l)$ is the probability that the diagonal length is l, and $p(l) = P(l)/\sum_{l \geq l_{\min}} P(l)$.

To sum up, for each IMF of the vibration signal, 12 features about the shape of the attractor trail and the recurrence plot matrixes are extracted. The dimension of the whole feature set is 84. Taking the signal in Figure 4a as example, all 84 features extracted based on VMD-PSR are shown in Table 3.

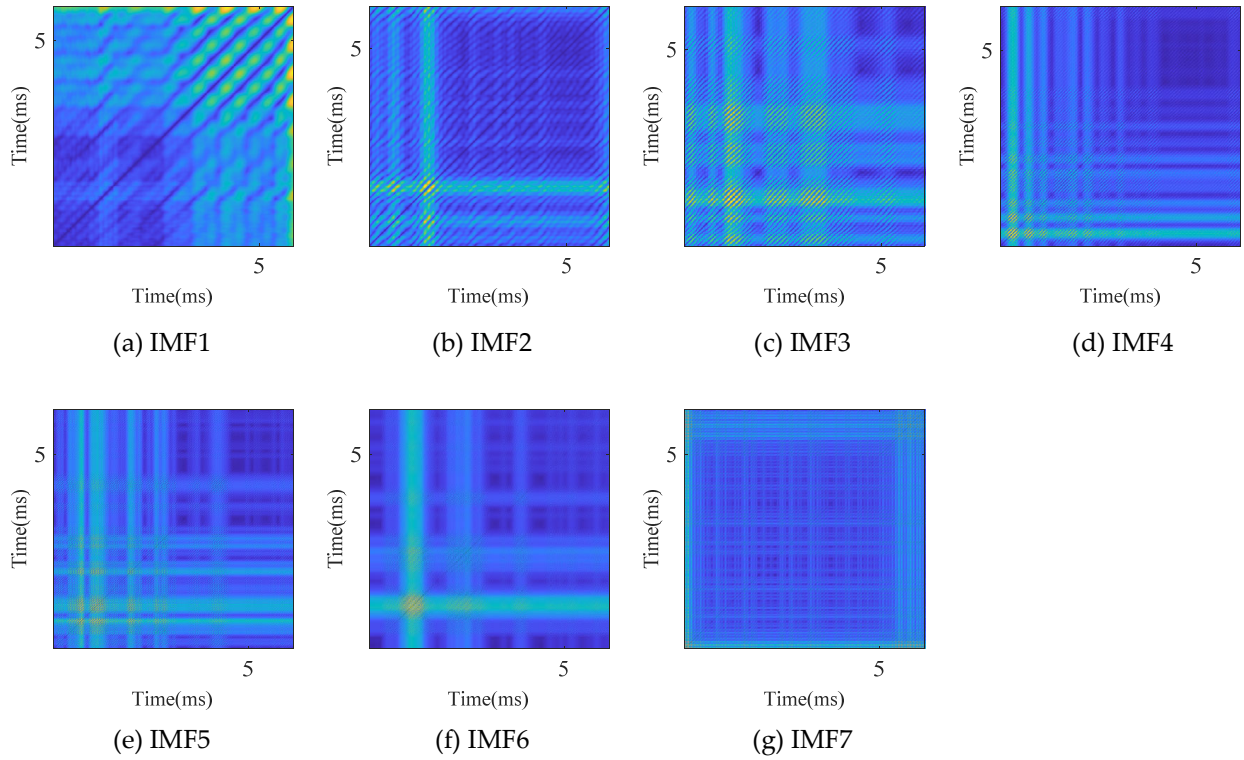

Figure 6. Recurrence plot images of the IMFs.

Table 2. Features from the shape of the recurrence plot matrixes.

Feature	Description
r_{r}	Recurrence rate, which represents the proportion of recursive points in the matrix. $r_{\mathrm{r}} = \frac{1}{N_0^2} \sum_{i,j=1}^{N_0} R(i,j)$
r_{det}	Determinism, which represents the proportion of the recursive points constituting the diagonal structure (excluding the main diagonal) in the matrix. $r_{\mathrm{det}} = \sum_{l=l_{\min}}^{N_0} lP(l) / \sum_{i,j=1}^{N_0} R(i,j)$
l_{d}	Average length of diagonal lines. $l_{\mathrm{d}} = \sum_{l=l_{\min}}^{N_0} lP(l) / \sum_{l=l_{\min}}^{N_0} P(l)$
s_{ent}	Shannon entropy of the diagonals. $s_{\mathrm{ent}} = -\sum_{l=l_{\min}}^{N_0} p(l) \ln p(l)$
r_{lam}	Laminarity, which represents the proportion of the vertical structure in the matrix. $r_{\mathrm{lam}} = \sum_{v=v_{\min}}^{N_0} vP(v) / \sum_{i,j=1}^{N_0} R(i,j)$
l_{tt}	Trapping time, which represents the average length of the verticals. $l_{\mathrm{tt}} = \sum_{v=v_{\min}}^{N_0} vP(v) / \sum_{v=v_{\min}}^{N_0} P(v)$

Table 3. Feature extraction results of vibration signal during the trip process.

Features	IMF						
	1	**2**	**3**	**4**	**5**	**6**	**7**
$r_{\max}$	25.366	39.994	34.145	39.325	14.374	27.554	1.465
$v_{\max}$	1.924	6.742	8.570	15.018	8.342	20.088	1.889
v_a	0.792	1.551	3.706	3.407	2.259	5.070	0.506
r_v	2.430	4.347	2.313	4.408	3.693	3.962	3.736
r_l	1.391	1.480	1.179	1.116	1.702	1.091	5.178
r_{s}	0.797	0.791	0.782	0.778	0.788	0.808	0.754
r_{r}	0.026	0.044	0.030	0.106	0.079	0.065	0.051
r_{det}	0.998	0.993	0.989	0.975	0.933	0.967	0.964
l_{d}	21.978	10.929	13.215	14.047	12.927	13.090	6.316
s_{ent}	3.383	3.001	3.127	3.170	3.096	3.246	2.430
r_{lam}	0.996	0.975	0.773	0.926	0.794	0.308	0.009
l_{tt}	7.689	4.805	4.633	5.764	3.403	2.959	2.125

3. Fault Simulation Test of the Trip Mechanism

The faults of the trip mechanism mainly include the coil-plunger jam, the open latch jam, and poor contact. Herein, the simulation test is carried out considering the following faults:

Fault1: jam between the coil and the plunger. By winding tape around the armature of the plunger, the radius of the core can be increased equivalently, so the resist force will be increased to simulate the jam fault.

Fault2: poor contact fault in the coil circuit. A 60 Ω resistance is connected in series with the coil circuit to simulate the fault.

Fault3: jam in the open latch. The obstacle is set to increase the moving resist force of the open latch, so as to simulate the jam fault.

Considering the dispersion of power supply voltage, the tests under the normal and fault1~fault3 conditions were carried out with the power supply voltage of 200, 210, 220, and 242 V, respectively. Under each power supply voltage, the tests were repeated 10 times. Herein, the vibration signals during the trip process were collected. Thus, 40 samples in normal state and each fault state are obtained, and the total number is 160.

The vibration signals under each fault are decomposed by the VMD method and the corresponding IMF1~IMF7 are obtained, which are shown in Figure 7. The results show that, when different faults occur, the IMF changes in different types. For the coil-plunger jam fault, owing to the increase in the resist force, the vibration signal generated by the coil is enhanced, so the amplitude and energy of IMF7 increase. For the poor contact fault, as the circuit resistance increases, the coil current as well as the acceleration of the plunger decrease, which lead to the decrease in the plunger speed and the low hit strength on the latch. Therefore, the amplitude and energy of each IMF, such as IMF4, are reduced. When there is jam fault in the open latch, the speed of the plunger decreases rapidly, and the hit on the latch is more intense, so the energy of IMFs in the low-frequency range increases. In addition, as the speed of the plunger is greatly reduced, the vibration generated on the coil is also greatly reduced, which leads to a greatly reduced amplitude of IMF7 as a result. To sum up, it can be seen that the changes in IMF under different faults show different characteristics, and fault identification can be realized by extracting features from these IMFs.

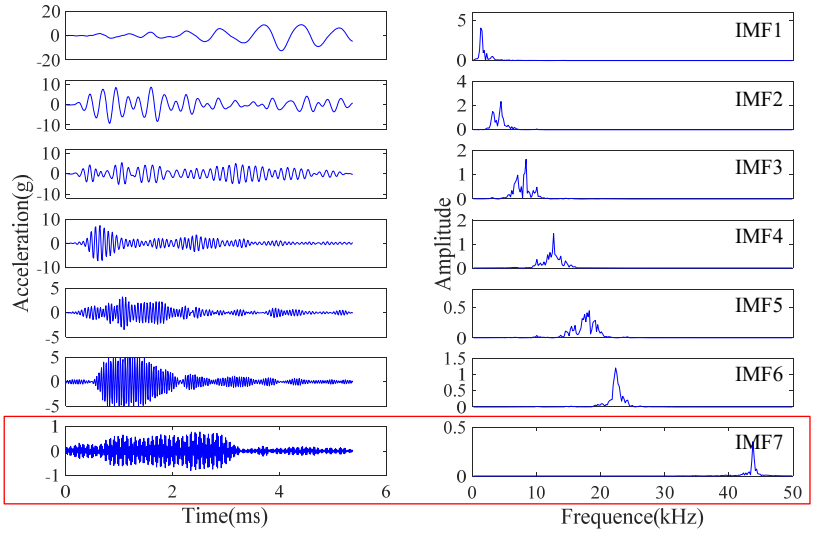

(**a**)

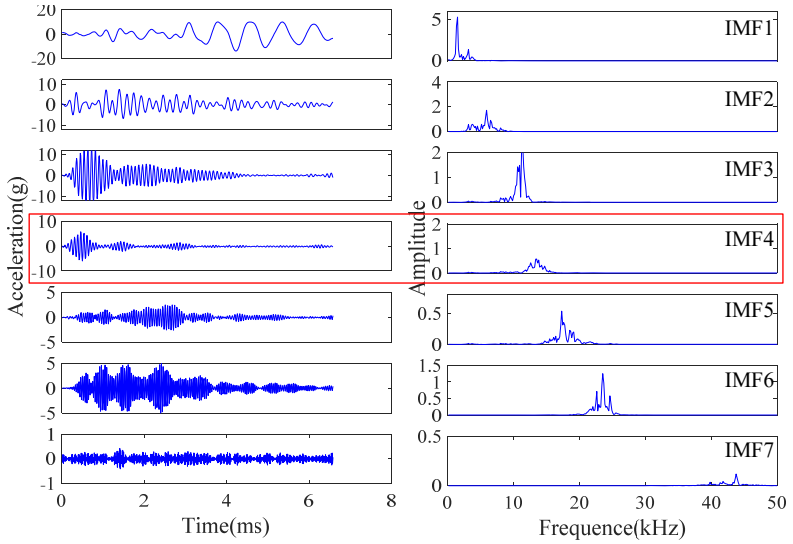

(**b**)

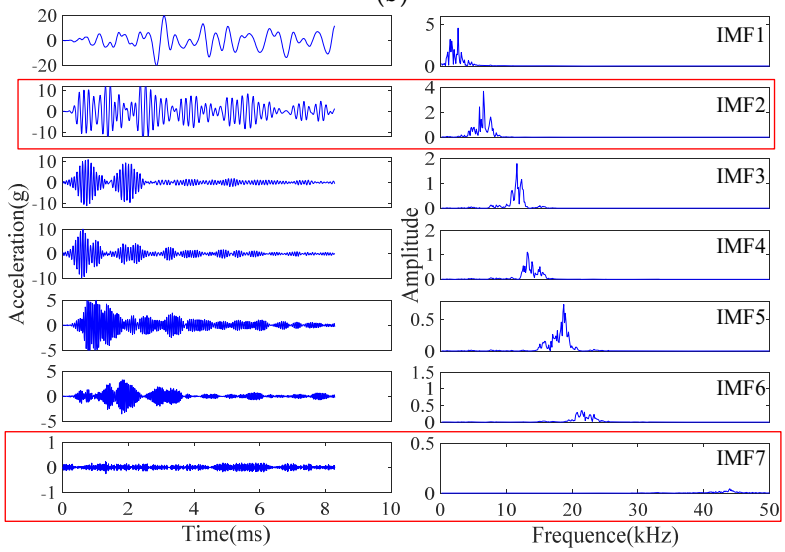

(**c**)

Figure 7. IMFs of the vibration signals under different faults. (**a**) Fault1 (coil-plunger jam). (**b**) Fault2 (poor contact). (**c**) Fault3 (jam in the open latch).

4. Fault Identification Model of the Trip Mechanism

4.1. Feature Extraction and Selection

The VMD-PSR method proposed in this paper is used to extract features from 160 samples obtained from the fault simulation test. Considering that there may be redundancy in the extracted 84-dimensional features, the feature set is optimized by correlation analysis. Pearson correlation coefficient is used to calculate the correlation degree between a feature and fault. For a certain type of feature, the correlation coefficient with a certain fault is calculated as follows:

$$r_{\mathrm{cor}} = \frac{\sum (x_i - \overline{x})(y_i - \overline{y})}{\sqrt{\sum (x_i - \overline{x})^2}\sqrt{\sum (y_i - \overline{y})^2}} \tag{16}$$

where x_i represents the feature value of the ith sample and $\overline{x}$ represents the mean value of the feature, while y_i represents the output value of the ith sample.

For binary classification problems, y_i is 0 or 1, and $\overline{y}$ is the mean value of the output. For the three faults involved in this paper, the binary sample sets of the fault sample and the normal sample are established, respectively, so as to calculate the correlation coefficient of each feature about the fault. The three-dimensional features with the highest correlation coefficient (l_{am} of IMF5, $r_{\max}$ of IMF7, and v_a of IMF1) are extracted, and the distributions of different fault samples in the feature space are shown in Figure 8.

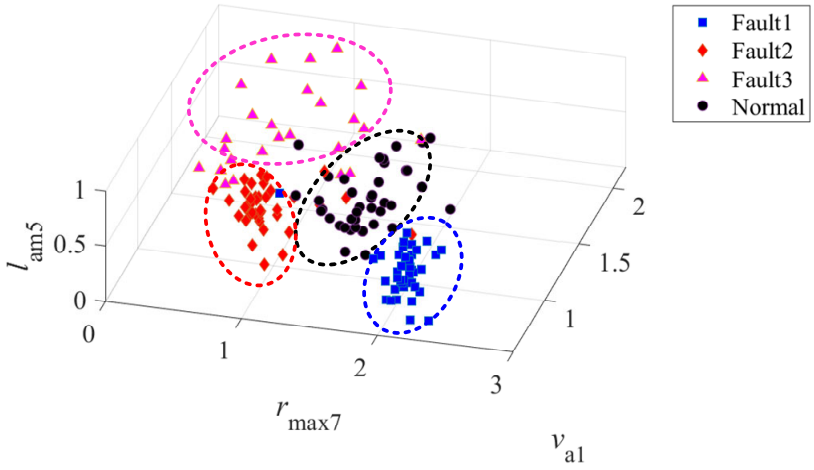

Figure 8. Distribution of samples in the feature space.

From the distribution of samples, it can be seen that samples of different faults have different distribution areas in the feature space. Normal samples are located in the middle of the feature space. When different faults occur in the trip mechanism, the features will change in different directions. Selecting features with a high correlation coefficient can effectively distinguish the fault samples. When the correlation coefficient $r_{\mathrm{cor}} > 0.4$, it can be considered that the feature is related to the fault. Therefore, the features with a correlation coefficient greater than 0.4 are selected as the feature set, with a total of 18 dimensions, which is shown in Table 4. IMF5 and IMF7 have the largest number of features related to the faults, which are the key signals to characterize the condition of the trip mechanism.

Table 4. Feature selection results.

IMF Component	Corresponding Features	Number
IMF1	v_{a1}, r_{l1}	2
IMF2	v_{a2}, r_{s2}	2
IMF3	l_{tt3}	1
IMF4	v_{max4}, v_{a4}, s_{ent4}	3
IMF5	r_{l5}, r_{r5}, r_{lam5}, l_{tt5}	4
IMF6	v_{a6}, r_{v6}	2
IMF7	r_{max7}, v_{max7}, r_{v7}, l_{d7}	4

4.2. Fault Identification Process

According to the results of the feature selection, the dataset is built and the fault identification research is carried out. A total of 20 samples are taken from normal and each fault data, respectively. Taking these 80 samples as the training sample set, the fault identification model of the trip mechanism is built. Then, the rest are used as test samples to verify the accuracy of the model. SVM could find the optimal classification hyperplane through the support vectors, so as to construct a mathematical model to solve the binary classification problem [28], which can be used to solve the small sample problem in this research. By introducing a penalty coefficient and kernel function, SVM can transform a nonlinear problem into a linear separable problem and limit the interference of noise samples. Radial basis function (RBF) has good generalization ability and is taken as the kernel function in SVM.

$$K(x, x') = \exp(-\gamma \|x - x'\|^2) \tag{17}$$

where γ is the kernel function parameter and x and x' are the input samples.

Before the training of the SVM model, each feature is normalized to eliminate the influence of different orders of magnitude and speed up the training and convergence of the prediction model. The normalization method is as follows:

$$x_i' = \frac{x_i - x_{\min}}{x_{\max} - x_{\min}} \tag{18}$$

where x_i' is the normalized value of the ith sample x_i in the sample set and $x_{\max}$ and $x_{\min}$ are the maximum and minimum value of the feature, respectively.

The penalty coefficient C and the kernel function parameter γ jointly determine the performance of SVM. In this paper, the grid search (GS) algorithm and cross validation (CV) method are used to find the optimal parameters (C, γ) [29]. The search ranges of C and γ are divided into equidistant grids by a certain step size, and all of the data points in the grid are traversed to calculate the classification accuracy under three-fold cross validation. Then, (C, γ) with the highest classification accuracy are taken as the optimal parameters in the subsequent SVM model. The whole fault identification process is shown in Figure 9.

4.3. Results and Discussions

The optimization ranges of penalty coefficient C and kernel function parameter γ are $[2^3, 2^9]$ and $[2^{-2}, 2^{-8}]$, respectively, and the search step is set to $2^{0.1}$. The optimization results are shown in Figure 10 and the optimal parameters are C = 8 and g = 0.0625. The SVM model is trained according to the optimal parameters and training set. The conditions of the test samples are predicted. In order to verify the effectiveness of the SVM model, BPNN (the number of hidden layers is 2, and the number of neurons is 10 and 4) and KNN (the value of K is set to 3) clustering algorithms are used to build identification models to predict the test samples, respectively. The results of these models are shown in Figure 11. Category 0 corresponds to the normal condition and categories 1~3 correspond to fault1~fault3.

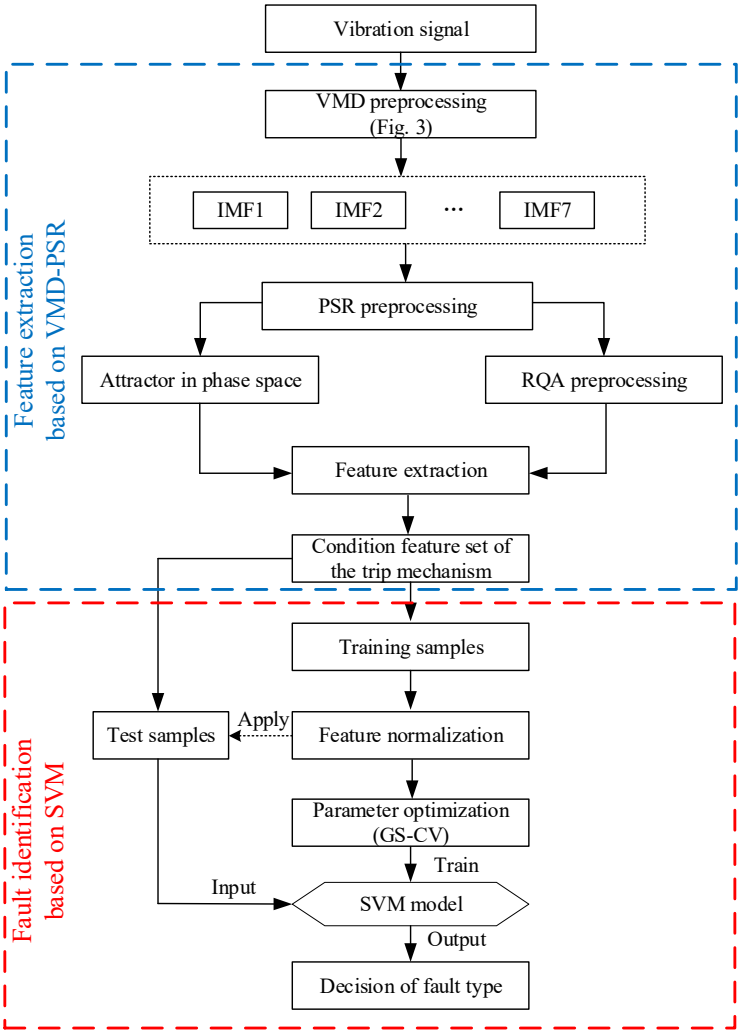

Figure 9. The fault identification process based on VMD-PSR and SVM.

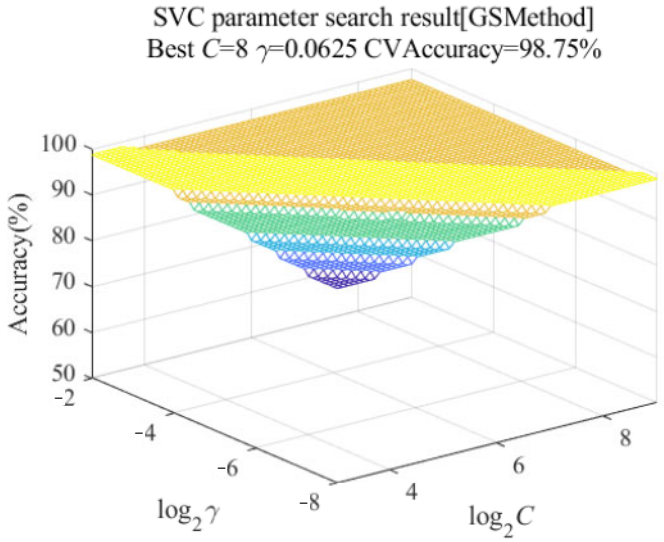

Figure 10. Parameter optimization results.

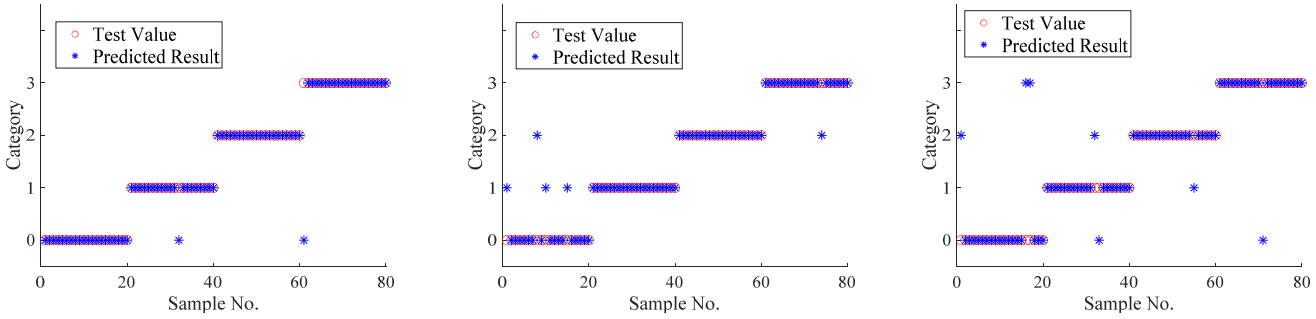

Figure 11. Fault identification results of different models. (**a**) SVM. (**b**) BPNN. (**c**) KNN clustering.

Obviously, there are 78 samples correctly identified in the SVM model, and the accuracy is 97.5%. Compared with other models, the accuracy of BPNN and KNN clustering models is 93.8% and 91.2%, respectively, verifying the effectiveness of the SVM model. In order to further compare the effects of the three identification models, the accuracy under each fault is evaluated by the F1 score, which considers both the precision and recall of the classification model. For a certain state (normal or a certain fault), the samples in this state are regarded as positive samples, while others are negative samples. The F1 score under this state is calculated by

$$R_{F1} = \frac{2R_{\text{pre}} \times R_{\text{rec}}}{R_{\text{pre}} + R_{\text{rec}}} \tag{19}$$

where R_{pre} and R_{rec} are the precision and recall, respectively, which can be calculated as follows:

$$\begin{aligned} R_{\text{pre}} &= \frac{TP}{TP + FP} \\ R_{\text{rec}} &= \frac{TP}{(TP + FN)} \end{aligned} \tag{20}$$

where n_{TP} is the number of positive samples with correct identification, n_{FP} is the number of negative samples predicted to be positive, and n_{FN} is the number of positive samples with negative results.

F1 scores of these three identification models for samples under different states are as shown in Table 5.

Table 5. Identification effect comparison of different models.

Category	Identification Model		
	GS-SVM	BPNN	KNN Clustering
0	95%	89%	87%
1	97%	93%	92%
2	100%	95%	93%
3	97%	97%	93%
Average accuracy	98%	94%	91%

According to the evaluation results of the F1 score, the average accuracy of these three models is more than 90%, which verifies the effectiveness of the feature extraction method proposed in this paper. Based on features from the VMD-PSR method, the condition of the trip mechanism can be effectively characterized, so as to realize the fault identification. Comparing the F1 scores of the normal sample set and various faults, it is shown that the F1 score of the normal sample set is lower than that of other faults. This is because, in the feature space, normal samples are located in the middle of other fault samples, which has a higher probability of confusion with other fault samples. When samples are classified by

hyperplane, normal samples will be surrounded by more hyperplanes, so more samples will be located near the normal-fault hyperplane, resulting in misclassification. In addition, the F1 scores of the GS-SVM model for normal state and various faults are all more than 95%, which is higher than the scores of the other two models. It is proved that the method is suitable for the small sample learning in this paper.

5. Conclusions

Aiming at the early faults in the trip mechanism of CBs, this paper proposes a feature extraction method from vibration signal based on the VMD-PSR algorithm. Based on the fault simulation test and SVM algorithm, the fault identification model is established and the effect of the model is verified. The following conclusions are obtained.

The vibration signal in the trip stage can be decomposed by the VMD method to obtain IMF components with different central frequencies. When the trip mechanism has different faults, the IMFs will change differently, which can be used as the basis for fault identification. Using the PSR method to mine the information of each IMF component, features of the attractor trail shape and the recurrence plot matrixes can be further extracted. Different fault samples are distributed in different regions in the feature space, which can be effectively distinguished by features with a high correlation coefficient. Using the SVM algorithm to build the fault identification model, the average identification accuracy is 98%, while the accuracy is also more than 95% for each fault. The method proposed in this paper can effectively identify the faults in the trip mechanism, such as the coil-plunger jam, poor contact, and open latch jam. It solves the difficulty in identifying early mechanical faults such as coil-plunger jam through the coil current. The research provides a new method for the fault identification of the trip mechanism, especially the open/close coils, which can provide a reference for the condition evaluation of CBs.

Author Contributions: Conceptualization, X.W. and J.R.; methodology, X.W. and Q.Y.; software, X.W. and Y.D.; validation, X.P. and T.Z.; experiments and data curation, X.P. and T.Z.; writing—original draft preparation, X.W.; writing—review and editing, Y.D.; project administration, J.R.; funding acquisition, Q.Y. All authors have read and agreed to the published version of the manuscript.

Funding: This research was funded by the Fuzhou Science and Technology Plan Project, grant number 2021-P-050.

Data Availability Statement: The data presented in this study are available on request from the corresponding author. The data are not publicly available due to privacy or ethical restrictions.

Conflicts of Interest: The authors declare no conflict of interest.

References

1. CIGRE Working Group A3.06. *Final Report of the 2004–2007 International Enquiry on Reliability of High Voltage Equipment*; CIGRE Technical Brochure 510; CIGRE: Paris, France, 2012.
2. Peng, Z.; Wang, S.; Yi, L.; Liu, Q.; Chen, X.; Liang, M.; Cao, C.; Yan, H.; Liu, D. Research on fault diagnosis of high voltage circuit breaker opening/closing coils based on SVM principal component analysis. *High Volt. Appar.* **2019**, *55*, 39–46.
3. Liu, Q.; Peng, Z.; Wang, S.; Yi, L.; Chen, X.; Chu, F.; Luo, T.; Liang, M.; Yi, M.; Liu, D. Fault current curves identification of circuit breaker opening/closing coil based on random forest algorithm. *High Volt. Appar.* **2019**, *55*, 93–100.
4. Cheng, C.; Chen, L.; Kao, W. Diagnosing medium voltage GIS circuit breaker by observing trip coil current with simulation and actual tests. *Electr. Power Compon. Syst.* **2008**, *36*, 181–194. [CrossRef]
5. Wang, X.; Ruan, J. A recognition method for the coil plunger motion resist force based on coil current in vacuum circuit breaker. *IEEJ Trans. Electr. Electron. Eng.* **2022**, *17*, 525–531. [CrossRef]
6. Razi-Kazemi, A.; Vakilian, M.; Niayesh, K.; Lehtonen, M. Circuit-breaker automated failure tracking based on coil current signature. *IEEE Trans. Power Deliv.* **2014**, *29*, 283–290. [CrossRef]
7. Ji, T.; Ye, X.; Shi, M.; Li, M.; Wu, Q. Typical current modelling and feature extraction of high voltage circuit breaker towards condition analysis and fault diagnosis. *IET Gener. Transm. Distrib.* **2020**, *14*, 1521–1527. [CrossRef]
8. Sun, S.; Zhang, T.; Li, Q.; Wang, J.; Zhang, W.; Wen, Z.; Tang, Y. Fault diagnosis of conventional circuit breaker contact system based on time–frequency analysis and improved AlexNet. *IEEE Trans. Instrum. Meas.* **2021**, *70*, 3508512. [CrossRef]
9. Gao, W.; Qiao, S.; Wai, R.; Guo, M. A newly designed diagnostic method for mechanical faults of high-voltage circuit breakers via SSAE and IELM. *IEEE Trans. Instrum. Meas.* **2021**, *70*, 3500613. [CrossRef]

10. Zhang, L.; Shi, D.; Miao, X. Research on vibration signal feature analysis and its fault diagnosis. *Electr. Mach. Control* **2016**, *20*, 82–87.
11. Charbkaew, N.; Suwanasri, T.; Bunyagul, T.; Schnettler, A. Vibration signal analysis for condition monitoring of puffer-type high-voltage circuit breakers using wavelet transform. *IEEJ Trans. Electr. Electron. Eng.* **2012**, *7*, 13–22. [CrossRef]
12. Huang, N.; Chen, H.; Cai, G.; Fang, L.; Wang, Y. Mechanical fault diagnosis of high voltage circuit breakers based on variational mode decomposition and multi-layer classifier. *Sensors* **2016**, *16*, 1887. [CrossRef]
13. Dou, L.; Wan, S.; Zhang, C. Application of multiscale entropy in mechanical fault diagnosis of high voltage circuit breaker. *Entropy* **2018**, *20*, 325. [CrossRef]
14. Dragomiretskiy, K.; Zosso, D. Variational mode decomposition. *IEEE Trans. Signal Process.* **2014**, *62*, 531–544. [CrossRef]
15. Abdoos, A. Detection of current transformer saturation based on variational mode decomposition analysis. *IET Gener. Transm. Distrib.* **2016**, *10*, 2658–2669. [CrossRef]
16. Yang, W.; Peng, Z.; Wei, K.; Shi, P.; Tian, W. Superiorities of variational mode decomposition over empirical mode decomposition particularly in time–frequency feature extraction and wind turbine condition monitoring. *IET Renew. Power Gener.* **2017**, *11*, 443–452. [CrossRef]
17. Ma, L.; Wang, G.; Zhang, P.; Huo, Y. Fault diagnosis method of circuit breaker based on CEEMDAN and PSO-GSA-SVM. *IEEJ Trans. Electr. Electron. Eng.* **2022**, *17*, 1598–1605. [CrossRef]
18. Zhao, S.; Wang, E. Fault diagnosis of circuit breaker energy storage mechanism based on current-vibration entropy weight characteristic and grey wolf optimization-support vector machine. *IEEE Access* **2019**, *7*, 86798–86809. [CrossRef]
19. Yang, Q.; Ruan, J.; Zhuang, Z.; Huang, D. Fault identification for circuit breakers based on vibration measurements. *IEEE Trans. Instrum. Meas.* **2020**, *69*, 4154–4164. [CrossRef]
20. Song, Q.; Jiang, X.; Wang, S.; Guo, J.; Huang, W.; Zhu, Z. Self-adaptive multivariate variational mode decomposition and its application for bearing fault diagnosis. *IEEE Trans. Instrum. Meas.* **2022**, *71*, 3503913. [CrossRef]
21. Kennel, M.; Brown, R.; Abarbanel, H. Determining embedding dimension for phase-space reconstruction using a geometrical construction. *Phys. Rev. A* **1992**, *45*, 3403–3411. [CrossRef]
22. Yang, Q.; Ruan, J.; Zhuang, Z. Fault diagnosis of circuit breakers based on time frequency and chaotic vibration analysis. *IET Gener. Transm. Distrib.* **2020**, *14*, 1214–1221. [CrossRef]
23. Webber, C.; Zbilut, J. Dynamical assessment of physiological systems and states using recurrence plot strategies. *J. Appl. Physiol.* **1994**, *76*, 965–973. [CrossRef] [PubMed]
24. Terrill, P.; Wilson, S.; Suresh, S.; Cooper, D.; Dakin, C. Attractor structure discriminates sleep states: Recurrence plot analysis applied to infant breathing patterns. *IEEE Trans. Biomed. Eng.* **2010**, *57*, 1108–1116. [CrossRef] [PubMed]
25. Niknazar, M.; Mousavi, S.; Vahdat, B.; Sayyah, M. A new framework based on recurrence quantification analysis for epileptic seizure detection. *IEEE J. Biomed. Health Inform.* **2013**, *17*, 572–578. [CrossRef]
26. Censi, F.; Calcagnini, G.; Cerutti, S. Proposed corrections for the quantification of coupling patterns by recurrence plots. *IEEE Trans. Biomed. Eng.* **2004**, *51*, 856–859. [CrossRef]
27. Marwan, N.; Romano, M.; Thiel, M.; Kurths, J. Recurrence plots for the analysis of complex systems. *Phys. Rep. Rev. Sect. Phys. Lett.* **2007**, *438*, 237–329. [CrossRef]
28. Vapnik, N. *The Nature of Statistical Learning Theory*; Springer: New York, NY, USA, 2000.
29. Qiu, Z.; Ruan, J.; Liu, C.; Jin, Q.; Huang, D. Discharge voltage prediction of complex gaps for helicopter live-line work: An approach and its application. *Electr. Power Syst. Res.* **2018**, *164*, 139–148. [CrossRef]